Imperviousness in Hungary's Second Largest City Using Spatial Analytics

Oluwatuyi S. Olowoyeye [1,2]

Erika Budayné Bódi [2]

1 Department of Agricultural and Biosystems Engineering, Iowa State University, Ames, IA.

2 University of Debrecen, Faculty of Agricultural and Food Sciences and Environmental Management, Institute of Water and Environmental Management, Böszörményi 138, 4032 Debrecen, Hungary.

Corresponding author: Oluwatuyi Sunday Olowoyeye

Email Address : olutuyi@iastate.edu

Data availability Statement

The authors confirm that the data supporting the findings are in the body of the research.

Conflict of Interest

All authors certify that they have no affiliations with or involvement in any organization or entity with any financial interest or non-financial interest in the subject matter or materials discussed in this manuscript.

Compliance with Ethical Standards

This paper complies with the ethical standards of research and methodology

Funding (optional)

The authors did not receive support from any organization for the submitted work.

Ethical Approval

Not Applicable

Informed Consent

Not Applicable

Abstract

Urbanization in Debrecen, Hungary, has rapidly developed buildings and infrastructure, replacing ecosystems like vegetation, forest, and farmland. This has created a high percentage of sealed-up land, which cannot absorb water leading to water quality impairment in nearby water bodies. This research aims to examine the degree of land imperviousness in Debrecen, Hungary, and its effect on stormwater movement. Properly handling impervious surfaces can prevent future disruptions, such as inundation caused by uncontained rainwater. The Normalized Built-Up Index was used for classification in the first analysis of the images, while the Linear Spectral Mixture Analysis (LSMA) was used for post-processing, resulting in an improved classification of built-up and non-built-up regions. The Sentinel 2020 had the highest recorded accuracy of 0.6, 0.243, and 0.059 for the R^2, Root Mean Square Error (RMSE), and Mean Square Error (MSE). Based on the predictions, 32.5 percent of the area is pervious. In comparison, 38 percent of the sampled locations display maximum imperviousness, resulting in a 50% runoff of precipitation per time, primarily in the city's center, where impervious surfaces such as roofs, driveways, parking lots, and roads are prevalent.

The results will help municipal planners and water managers make educated choices about sealed land and its impact on stormwater movement, particularly during these shifting climatic conditions.

Keywords

Land use, climate change, remote sensing, waterways, runoff.

Abbreviation

Normalized Built-Up Index - NDBI

Linear Spectral Mixture Analysis - LSMA

Root Mean Square Error RSME

Mean Square Error MSE

Highlights

The level of imperviousness could be determined using spectral imagery analytics.

Sentinel is better used in knowing trends of imperviousness due to higher resolution.

Linear spectral mixture analysis methods are better used with high-resolution spatial imageries.

Land imperviousness is a precursor to low infiltration and uncontrolled stormwater flow.

Planning land development would limit the increasing rate of land imperviousness all over the world.

1.0 Introduction

Today, the world is experiencing a global increase in urban areas, leading to widespread changes in land surfaces over time (Seto et al., 2012; Nowak and Greenfield, 2020). People are gravitating toward the cities because of the infrastructure and basic amenities; As a result of increasing population, there is rapid infrastructure development which has negative environmental impact (Wauters, 2017; D'Acci, 2021). Also, as urbanization continues to take place, greenhouse gas release will increase in the city due to the multiplicity of available automobiles and heavy-duty equipment (Jyoti and Vibhooti, 1995). Furthermore, the loss of vegetations and tree canopies will be the order of the day since more regions will be developed, animal populations will be inhibited, and the wild will go extinct.

Urbanization requires replacement of natural vegetations with concrete development, glass, plastic and tarmac. One of the consequence of these are impervious surfaces which do not allow smooth water flow resulting in numerous environmental hazard risks, such as an excess stormwater flow that could eventually result in flash flood activities (Browne et al., 2021). Impervious areas also includes regions where infiltration is impossible or limited. Imperviousness varies based on locations, weather conditions, and soil type. Land areas with more vegetations, rainfall is absorbed into the soil through infiltration and is further stored as groundwater, and flooding is always less evident because the runoff is gradually discharged into the streams through seeps (Bradshaw, 2007; Bathurst et al., 2018).

As water movement occurs after rainfall, and no material medium absorbs it, the flow persists and accumulates, causing high-level stormwater flow, which could surge beyond natural order events (Hawley and Bledsoe, 2011; Braud et al., 2013). The water quality of nearby rivers also becomes compromised because of limited purification and reduced groundwater recharge (McGrane, 2016).

Several hydraulic structures had been put in place to reduce the aftermath of imperviousness in terms of stormwaters. Horvath et al., 2009b developed a numerical weather prediction model MM5 which could predict a storm; this is a pointer to the fact that weather has contributed in a significant way to how stormwater flows through an impervious layer; this is seen through the vegetation and soil in the region as established by Hovath et al. (2009a). Rather than using corrective measures through machines, a critical study of imperviousness could activate preventive measures.

Various methods have been employed to extract impervious surfaces to understand urban environments better (Estoque and Murayama, 2015; Fox et al., 2019). These techniques can be classified into different categories. The first category involves the use of spectral unmixing techniques (Xu et al., 2018), which assume that the modeled surface reflectance is a combination of spectra from distinct ground components. This type of analysis provides insight into the actual fractional components present on the ground.

Another category deals with the Artificial Neural Network to determine the fractional coverage for different land cover types based on the regression/decision tree method; this is established through an empirical model used for the prediction (Prasada and Wu, 2007; Hoang, 2021). The last category is object-based analysis, which uses high-resolution images to determine the percentage of impervious surfaces with extraction dependent on the image's spectral, spatial, and texture characteristics (Wei, 2018).

In assessing this impervious surface through indices, several data have been used in their analysis and extraction, and the primary intention is to have images with high resolutions, which makes the extraction of the impervious surface easy. Some of the data are retrieved from Landsat 8 Operational Land Imager (OLI), Mapper/Enhanced Thematic Mapper Plus(TM/ETM+) (Lakshmi et al., 2015, Ma et al. 2021) when it comes to apparent advantages of providing direct observation of the forest canopy system in the vertical plane. LiDAR has been recognized as the most effective instrument in the mapping of large-scale forest canopy height (Li et al., 2020); so many other data has been used for the analysis of land use/land cover and the rate of imperviousness, such as Moderate Resolution Imaging Spectroradiometer (MODIS), Advanced Spaceborne Thermal Emission and Reflection Radiometer (ASTER) (Duan et al., 2017), and Sentinel.

Sentinel stands out because of its uniqueness of 10 m resolution per pixel of the imagery, having 13 spectral bands spanning from the visible and near-infrared to the shortwave infrared (Xu et al., 2018; Kuc and Chormański, 2019). This research would adopt the use of both Landsat and Sentinel satellite data imagery to calculate and find the level of imperviousness using the Normalized Built-up Index (NDBI) and Linear Spectral Mixture Analysis (LSMA); the indicator would be used to predict the stormwater level. The research aims to analyze the urban imperviousness in the eastern part of Hungary using Debrecen as a case study; in the process explores the NDBI and LSMA methods of imperviousness extraction and compares the output for the two processes and draws inferences for stormwater flow in the city. Moreover, a regression model was used for comparison, as it is an effective statistical tool for determining the degree of correlation between two variables. Using this approach in the study, we were able to estimate the impact of imperviousness on the flow rate of stormwater, which can inform urban planners and water managers in their efforts to mitigate the adverse effects of urbanization on the natural hydrological cycle.

2.0 METHODOLOGY

2.1 Study Area

Debrecen in eastern Hungary is chosen as the target research area; it is the second-largest city in Hungary after Budapest. Debrecen is the regional center of the Northern Great Plain region and the seat of Hajdú-Bihar county as shown Fig.1. It was the largest Hungarian city in the 18th century, and it is one of the most important cultural centers of the Hungarians. Geographically, the area lies between 21° 37' E to 59.99" E longitudes and 47° 31' N and to 59.99" N latitude bordered to side by Hajusamson, Hadjuboszormeny, Bocskaikert, Vamospercs, Derecske, Hajduzboszlo, and Balmzujvaros. The population of 204,124 living in it over a 471.7 km^2 area. The mean annual precipitation totals 560 mm per year. July is the hottest month in Debrecen, with an average temperature of 20°C (68°F), and the coldest is January at -2°C (28°F). The wettest month is June, with an average of 80 mm of rain.

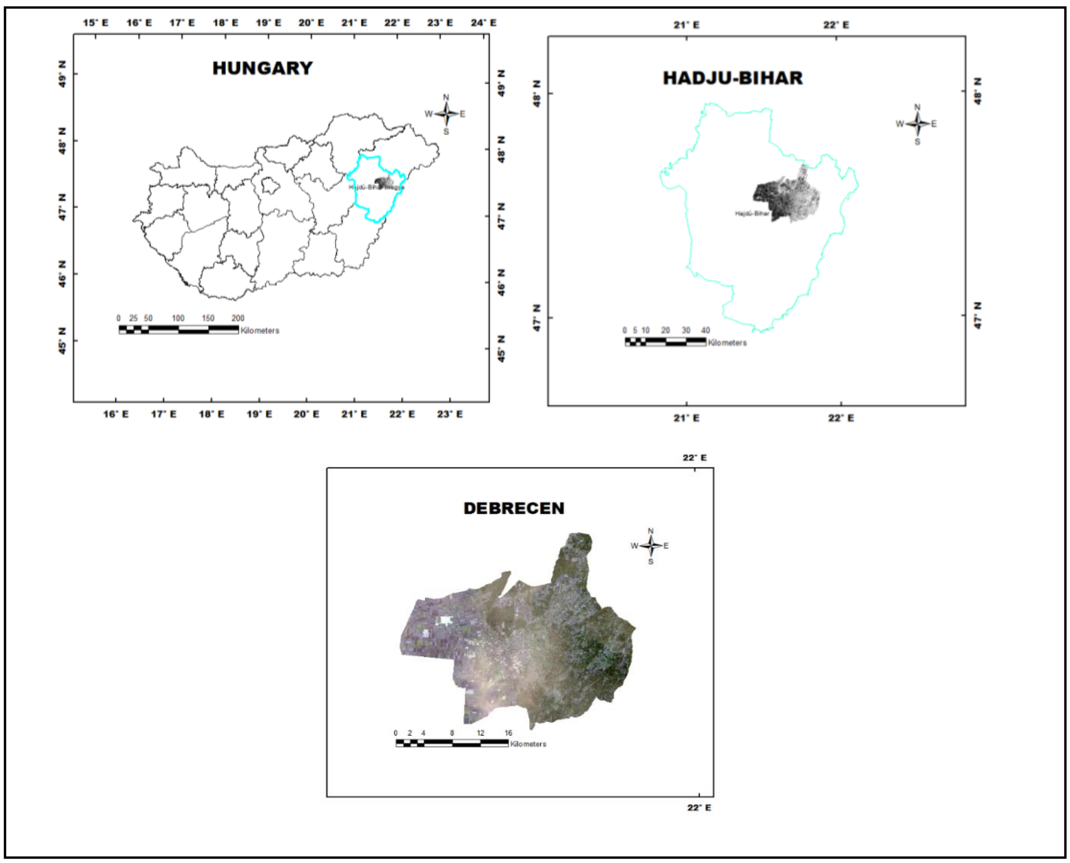

Fig. 1. Map of study area showing the country, county, and city.

2.2 Landsat OLI imagery

We have made the choice of Landsat and Sentinel as a resource to get data because they are readily available and free to use, they also both have historical data that would be valuable in understanding the changes that has happened over the years. In the analysis of the imperviousness rate, multispectral imagery data was deployed. The Landsat multispectral imagery (Operational Land Imager (OLI) and Thermal Infrared Sensor (TIRS)) was collected to analyze the imperviousness in the Debrecen region between 2013 and 2018. Landsat measures the radiance reflected from the earth 9 spectral bands for OLI and the remaining for the TIRS sensors; as shown in table 1, each of the bands has resolutions of 30m except for TIRS, which is 15, 30, and 100m, respectively. They have been used for land change detection maps, and land use land cover to analyze the impervious layer (Xu *et al*., 2016).

Table 1: Landsat 8 OLI/TIRS band specification

Band	Description	Wavelengths (nm)	Resolution (m)
1	Blue	430–450	30
2	Blue	450–510	30
3	Green	530–590	30
4	Red	640–670	30
5	Near Infrared	850–880	30
6	Shortwave Infrared (SWIR 1)	1,570–1,670	30
7	Shortwave Infrared (SWIR 2)	2,110–2,290	30
8	Panchromatic	500–1,380	15
9	Cirrus	1,360–1,380	30
10	Thermal Infrared	10,600–11,190	100
11	Thermal Infrared	11,500–12,510	100

Source: Estoque and Murayama (2015)

2.3 Sentinel-2A/ L2A image

For optimal accuracy through comparison, sentinel 2A level-2A multispectral imagery was also collected to analyze the imperviousness in the Debrecen region for the years 2019 and 2020. Sentinel 2 measures the radiance reflected from the earth in thirteen spectral bands, each of the bands as shown in table 2, including the Visible and Near-Infrared (VNIR) and Shortwave Infrared (SWIR), the bands cover a range of 440nm to 2190nm. With a swath width of 290 km and a spatial resolution of 10 m (four visible and near-infrared bands), 20 m (six red edge and shortwave infrared bands), and 60 m (three atmospheric correction bands). Sentinel two imagery has the capacity for coverage of generic land cover, land use, and change detection maps, which makes a good option for analysis of impervious layer.

Table 2: Sentinel-2 MSI Band Specification

Band	Description	Wavelengths (nm)	Resolution (m)
1	Coastal aerosol	433–453	60
2	Blue	458–523	10
3	Green	543–578	10
4	Red	650–680	10
5	Vegetation Red Edge (RE1)	698–713	20
6	Vegetation Red Edge (RE2)	733–748	20
7	Vegetation Red Edge (RE3)	773–793	20
8	Near-Infrared (NIR)	785–900	10
8a	Narrow NIR (nNir)	855–875	20
9	Water vapor	935–955	60
10	Shortwave infrared - Cirrus	1360–1390	60
11	Shortwave infrared (SWIR1)	1565–1655	20
12	Shortwave infrared (SWIR2)	2100–2280	20

Source: Xu et al. (2018)

2.4 Using NDBI to extract impervious layer

One of the most crucial land cover indexes for extracting urban data such as impervious surfaces is the NDBI. The NDBI image is a single-band gray-level image that emphasizes urban specifics rather than distinguishing between urban and non-urban groups (binary image). It creates a thematic map of impervious surfaces from an NDBI image, and the appropriate threshold value was chosen and then applied to separate impervious and non–impervious areas (Sekertekin and Zadbagher, 2021).

The NDBI was extracted to determine built-up areas from the Landsat and Sentinel multispectral spectral imagery, and this was integrated with Otsu's method, which automatically sorts the optimal threshold based on the observed distribution pixel values. The NDBI was calculated using the near-infrared band (NIR) and shortwave infrared band 1 (SWIR) as shown in the equation below:

$$NDBI = \frac{\rho SWIR1 - \rho NIR}{\rho SWIR1 + \rho NIR} \qquad 1$$

The algorithm from Otsu's thresholding method (Otsu, 1979) was used alongside the NDBI; this for image processing of the data extracted from the Sentinel, various threshold values was calculated to know the spread of the pixel levels relative to the threshold within the weighted class variance. The analysis was carried out on the ArcGIS, and it automatically assigns binary function, which is either 0 and 1; the system records one as the foreground and the other as the background. The built-up pixel detected for this analysis got assigned to NDBI value greater than 0 and other pixels are taken to be the pervious layer. It has been used to increase the accuracy of built-up areas. The mathematical formula for Otsu's method is as shown in Equation 3.7 – 3.10.

$$\sigma^2 = P_{nu}, \cdot (M_{nu} - M)^2 + Pu \cdot (M_u - M)^2 \qquad 2$$

$$M = P_{nu}. M_{nu} + P_u \cdot M_u \qquad 3$$

$$Pnu + Pu = 1 \qquad 4$$

$$\underset{a \le t \le b}{argmax}[P_n . P_{nu} . (M_u - M_{nu})^2 \qquad 5$$

Where σ is the interclass variance, M is the mean value of the NDBI image, P_{nu} and P_u are the percentages of non-built-up and built-up pixels, respectively, M_{nu} and M_u are the mean values of non-built-up and built-up pixels of the NDBI image, respectively, and t is the optimal threshold.

2.5 Linear Spectral Mixture Analysis

After the extraction has been done using the NDBI, the built-up and not built-up index cannot accurately be said to be perfect, and the classification also considered bare land as a built-up, hence the need for the linear spectral mixture analysis. Assumptions are made that a finite set of endmembers linearly mixes the image, endmembers considered were impervious and pervious surface, and their resulting fractions were calculated using the

$$Ri = \sum_{k=1}^{n} f_{k.} R_{ik} + \varepsilon_i \qquad 6$$

$$\sum_{k=1}^{n} f_{k.,} = 1, f_{k.} = 0 \qquad 7$$

In spectral data discovery, LSMA is a commonly used theory. The process begins by assuming that a data sample can be modeled as a linear admixture of a finite range of simple material substances, from which the data sample can be unmixed into their respective abundance fractions. In this case, analysis of the data sample can simply be performed on these abundance fractions rather than the sample itself. The technique that realizes this LSMA is generally known as Linear Spectral Unmixing (LSU). Endmembers play a critical role in achieving the LSMA. This fixed set of images linearly mixes sampled data for analysis. After then, each feature is identified and unmixed relative to the abundance fractions of the end members (Chang, 2016)

2.6 Accuracy assessment

After the data had been analyzed through the LSMA to ascertain the authenticity of data extracted from the imagery, it was subjected to reference information on imperviousness from the Copernicus; it is a composition of High-Resolution Layer (HRL) imperviousness for the year 2018 but modified to capture significant changes till 2020. This HRL imperviousness data was first compared to ground truth data from google earth images (Xu et al., 2016).

For these first stages, 100 locations were sampled for analysis simultaneously to consider the places with buildings, roads, parking lots, asphalt, bare land, vegetation, and forested regions. From close monitoring and observation, if the image from both google earth and imagery on ArcGIS Pro indicates they are pervious or impervious, values 0 and 1 are assigned, respectively, but if it is a mix of the two or could not easily be detected. The high-resolution imagery samples were taken from google earth, with a predetermined area for each sample; a placemark to further establish the region of interest was placed on the four different points at the extreme of the images. They were converted to degrees and decimal minutes; this was processed into the keyhole markup language zipped with additional images exported into ArcGIS, where they were georeferenced. Measurements were done using the impervious layer relative to the area of study for each of the samples.

The image retrieved from google earth is not georeferenced to enable effective mensuration and make the internal coordinate system of an image correlated to the ground system of geographic coordinates. Each of the images was preprocessed on the ArcGIS, and control points were used to map designated placemarks together and register the image under the Universal Transverse Mercator (UTM) 1984 for Debrecen; this process was repeated for sampled image access as described in Fig. 2.

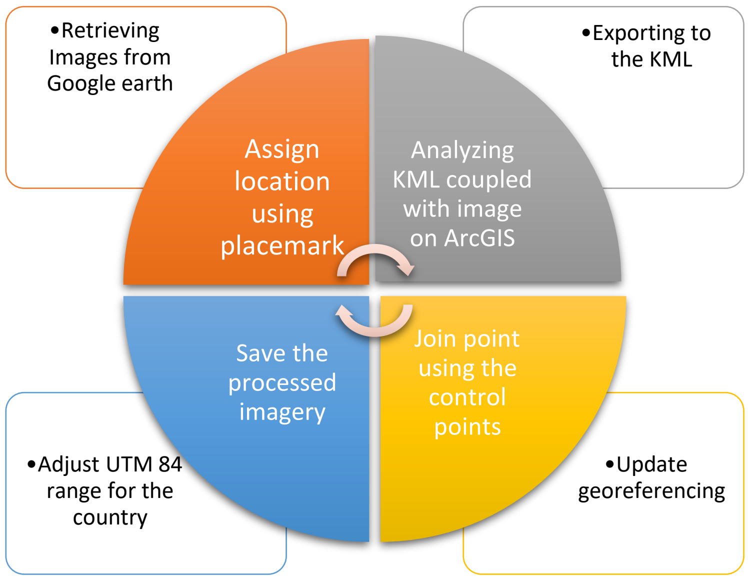

Fig. 2. Flow chart for Georeferenced Image from Google Earth

After the degree of variability had been established, 200 locations were sampled randomly from the HRL imperviousness data and were suitably compared to the 10 imageries from both Sentinel and Landsat, respectively.

The estimated imperviousness of the randomly sampled point from HRL was compared to the one from the indexes, and it was evaluated to check the model's accuracy. The MSE, MAE, RSME and R-square metrics consider associated error with the output and help to know the strength of the model.

$$MAE \frac{1}{N}\sum_{i=1}^{N}|y_{i}-\hat{y}| \qquad 8$$

$$RSME = \sqrt{MSE} = \sqrt{\frac{1}{N}\sum_{i=1}^{N}(y_{i-}\hat{y})^2} \quad 9$$

$$R^2 = \frac{\sum(y_{i-}\hat{y})^2}{\sum(y_{i-}\bar{y})^2} \quad 10$$

$where, \quad \hat{y} - predicted\ value\ of\ y$

$\bar{y} - mean\ value\ of\ y$

2.7 Imperviousness and stormwater flow estimation

The level of imperviousness was extracted based on different multispectral imagery, the one that gives the highest was used to estimate possible stormwater flow in the city. Afterward, the result was extracted based on a comparative analysis of stormwater flow with values from the EPA to check the rate of imperviousness relative to the expected water stormwater flow. The result was expressed in five classes namely, 0-20%, 20-40%, 40-60%, 60-80%, 80-100%. The class in the range of 0-20% completely pervious area of land, which is mostly forested or grassland region, the middle class 20% - 80% is a mesh of both pervious and impervious, with increasing order of imperviousness till 80% while the class of 80-100% is an impervious area of land that is mostly building, pavement, and roads.

3.0 RESULTS AND DISCUSSION

The level of imperviousness in the Debrecen region was analyzed using the Normalized Difference Built-Up Index (NDBI) technique on satellite imagery data from different years. For the 2020 Sentinel data, the highest and lowest threshold values were 0.999214 and -0.567084, respectively, while for the 2019 data, the values were 0.999809 and -0.69967, respectively. The NDBI values for Landsat OLI data from 2013 to 2020 were also examined, with values ranging from 0.50817 to 0.8025 for built-up regions and -0.0712 to -0.1131 for non-built-up areas. Fig. 3-5 depict the distribution of built-up and non-built-up areas, with positive values indicating built-up areas and negative values depicting non-built-up areas.

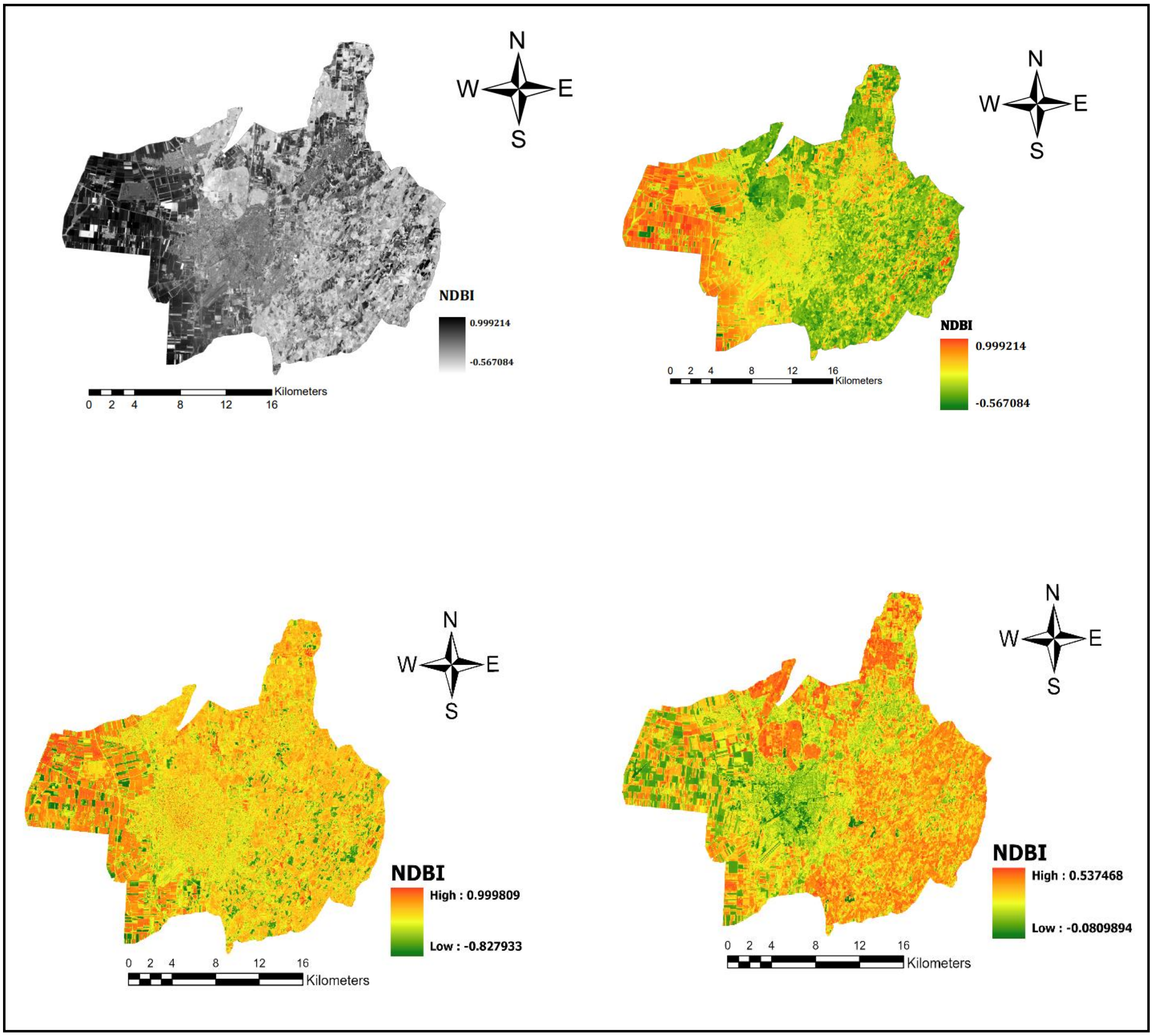

Fig. 3. Normalized Built-Up Index (NDBI) for imagery of Sentinel 2019, 2020 and Landsat 2020

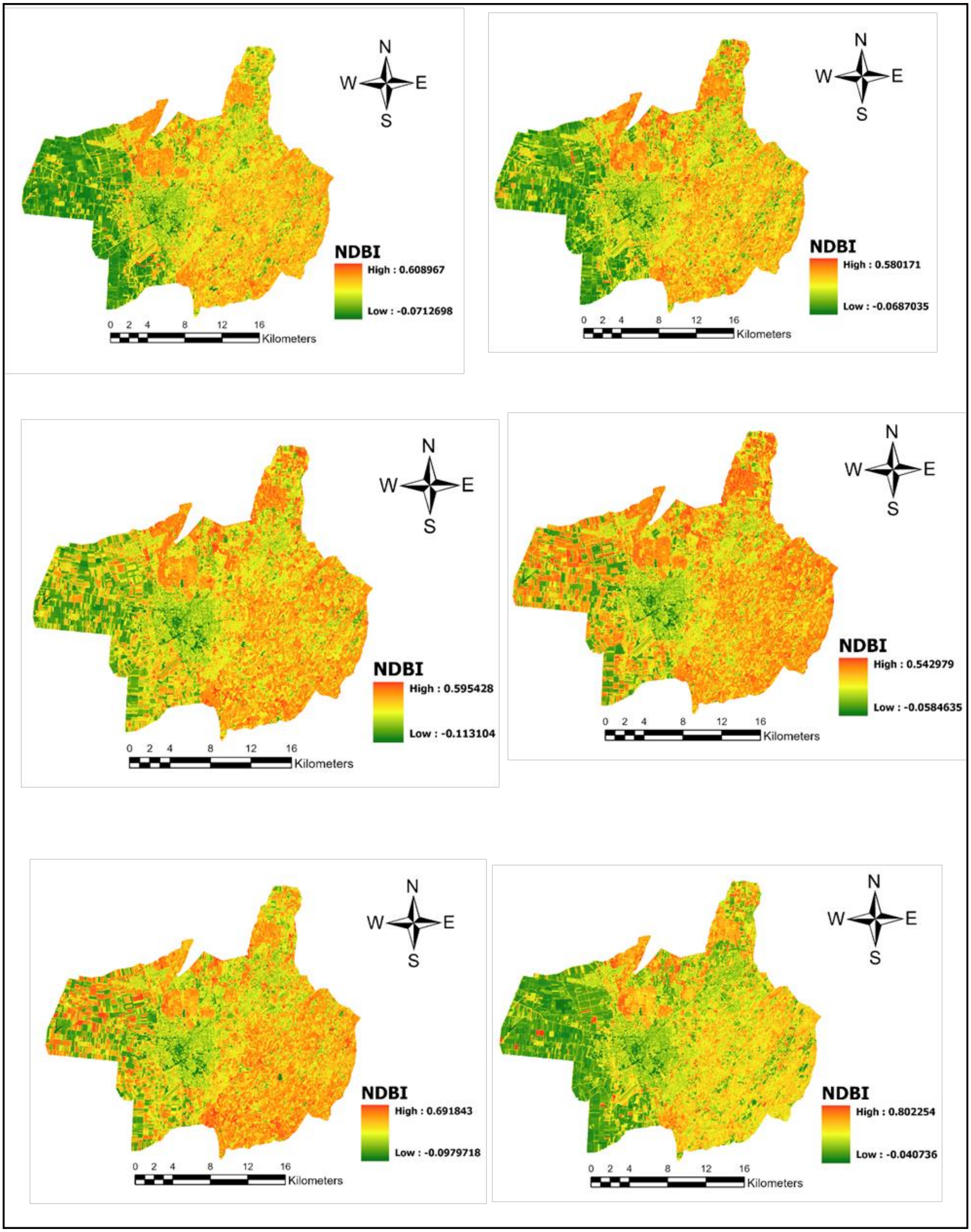

Fig. 4. Normalized Built-Up Index (NDBI) for imagery of Landsat 2019, 2018, 2017, 2016, 2015, 2014

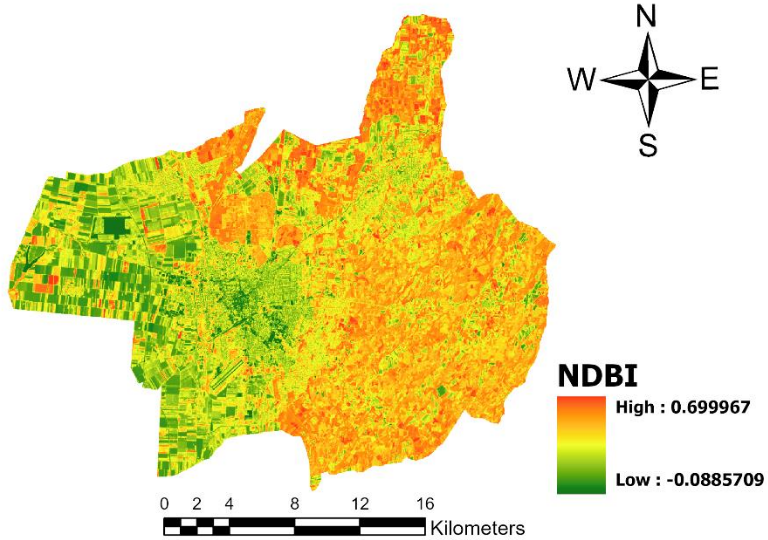

Fig. 5. Normalized Built-Up Index (NDBI) for imagery of Landsat 2013

These showed the range of imperviousness based on the built-up and the and non-built up; for the sentinel data in both years, the built-up index value is on the high side, this could easily be attributed to the 10m resolution as it captures more details against that of Landsat data which is 30m resolution. Random samples mapped out from NDBI results using the pixel of a different city region showed variation relative to the other samples as shown by the histogram displayed in Fig. 6-8; they were converted to the percentage value of the index.

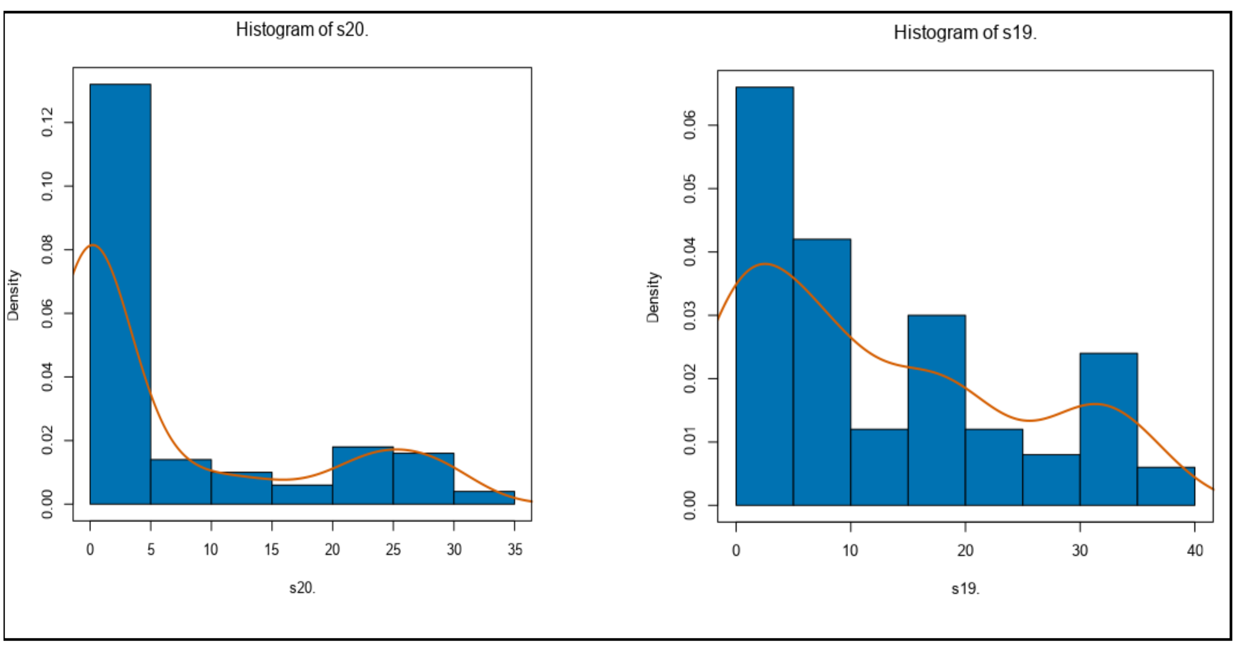

Fig. 6. Histogram showing the value of imperviousness extracted from NDBI result for Sentinel 2020(s20) and Sentinel 2019(s19)

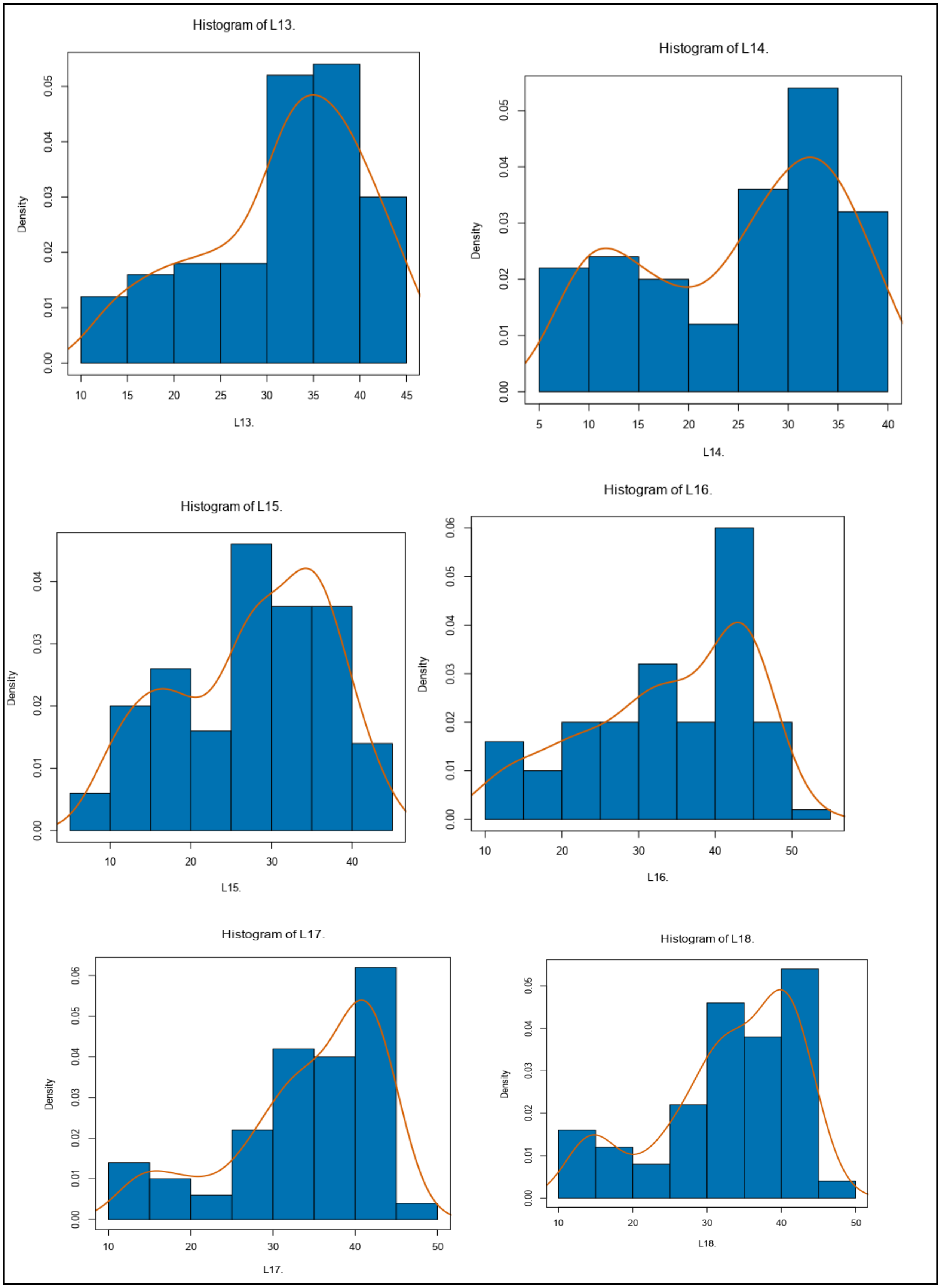

Fig. 7. Histogram showing the value of imperviousness extracted from NDBI result for Landsat 2020(L20), Landsat 2019(L19) , Landsat 2018(L18), Landsat 2017(L17), Landsat 2016(L16), Landsat(L15).

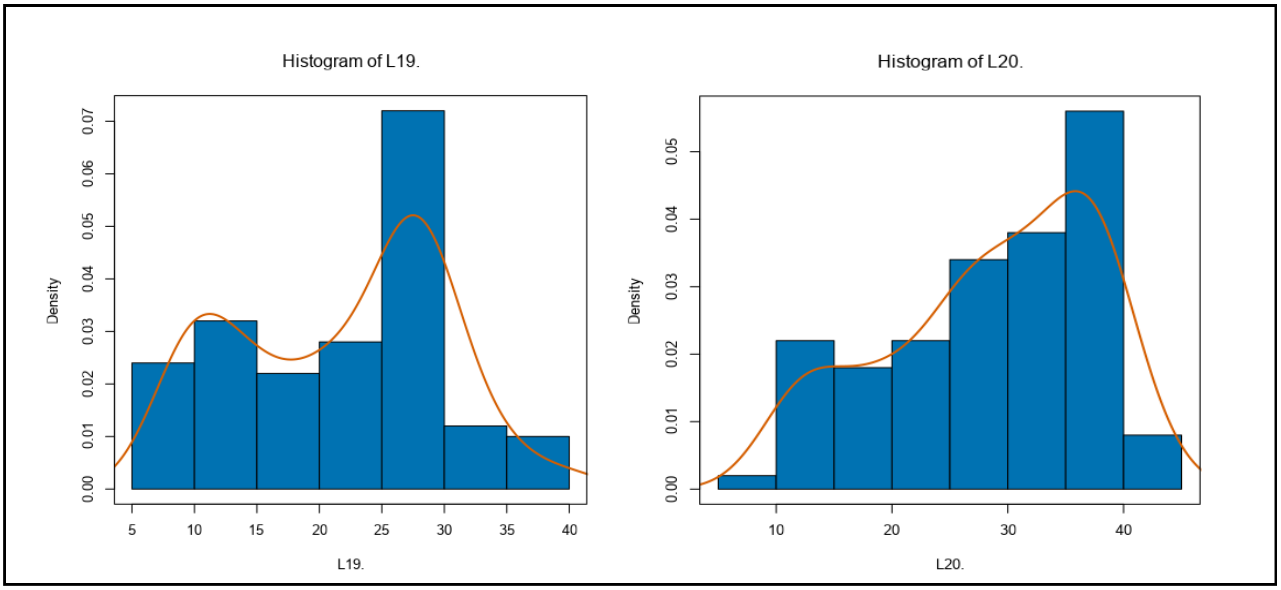

Fig. 8. Histogram showing the value of imperviousness extracted from NDBI result for Landsat 2014(L14), Landsat 2013(L13) .

The threshold values in Fig. 6-8 showed a higher range than the pixel value extractions, the highest possible for both Sentinel and Landsat in all the years was 50.87%. The result showing on the random histogram sampling shows that the Sentinel for 2019 and 2020 tends to have the highest value between the range of 0% and 5%. In Landsat data, the trends showcase imperviousness between 20% and 30% dominant in the representation. There is an observed relationship between most of the data; for Landsat of 30m resolution and the Sentinel of 10m resolution, there are some levels of correlation between the values.

3.1 Otsu Binary thresholding

Reclassification was carried out using the Otsu method showed misclassification in the analysis for better insight into the data. The NDBI assumed that most areas with low albedo are built-up as well, the area with bare land. The west side of the city with mid and large-sized cropland mainly on chernozem soil (Hajdúság), while the north side of the city with smaller pastures, gardens, yards, and smaller croplands on sandy soil (Nyírség), and the east side which is forests and forest steppes, with a balanced mix of the two on sandy-loamy soil (Dél-Nyírség) all, were regarded as built up as shown in Fig. 9 and 10.

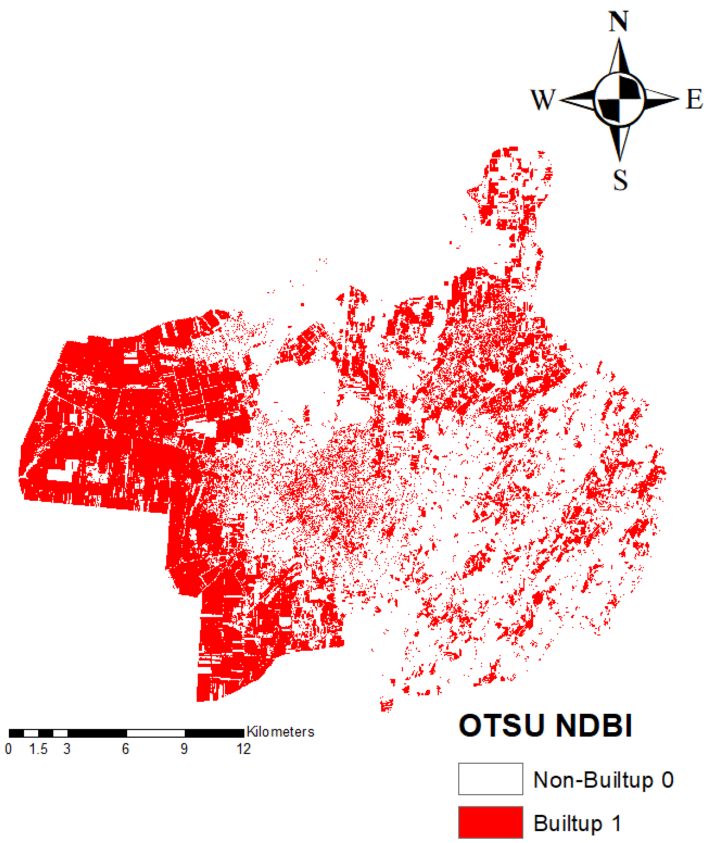

Fig. 9. Non-built-up (white) and Built up(red) extracted from the Otsu method for Imagery of Sentinel 2020

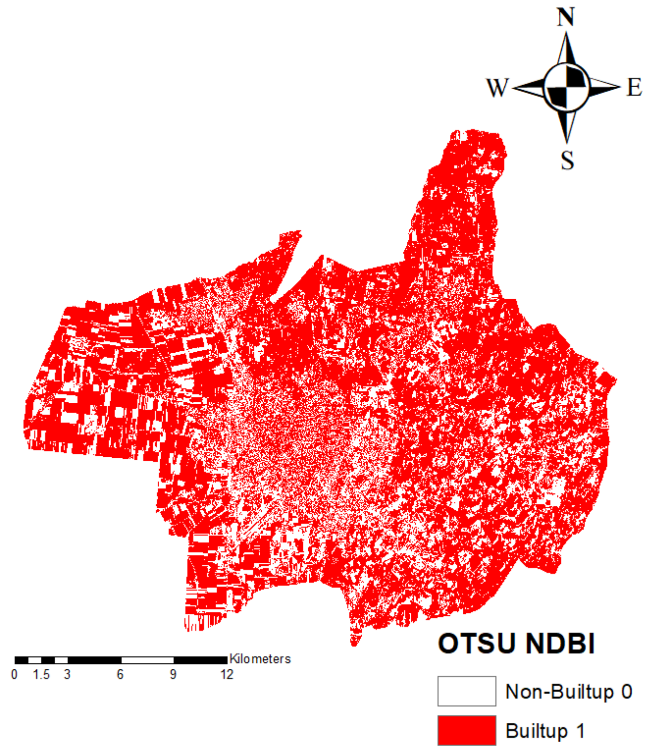

Fig. 10. Non-built up(white) and Built-up(red) extracted from Otsu method for Imagery of Sentinel 2019

From the output as shown in Fig. 9 and 10, only the 2020 sentinel data showed a different spectral mixture of both the built-up and the non-built-up; for 2019, the non-built-up were not well represented in the result. Representation of the dataset from Landsat using the OTSU was not possible because the threshold index value for the Landsat data is in the range of -0.01 and 0.1. It returned the value primarily as 1, making the image become blank void of variety.

3.2 Linear Spectral Mixture Analysis (LSMA)

The Linear Spectral Mixture Analysis (LSMA) used to gain insights into the data further showed higher accuracy than the NDBI; the satellite's masking aided classification to know where water bodies are located, as shown in Fig. 11. It was achieved using the Modified Normalized Water Index, and the surface is automatically characterized with the white and location different variable output in the shade of black.

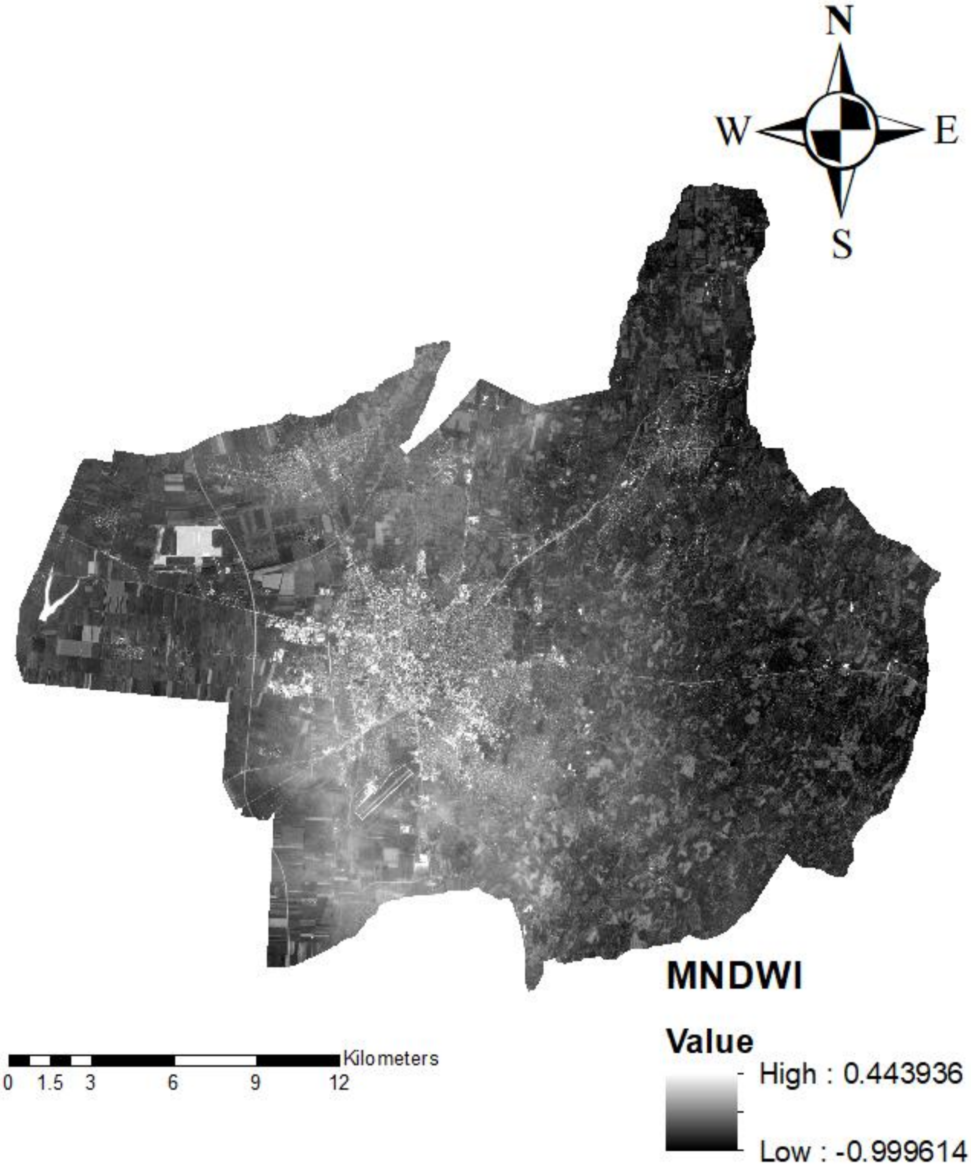

Fig. 11. Water bodies(white) and others (grey and dark) extracted from Modified Normalized Difference Water Index Sentinel 2020

After digitizing imagery based on the chosen endmember with significant consideration for the dataset from HRL Copernicus, the spectral mixture analysis carried showed improved classification of the output is as shown in Fig. 12-21. From observation, the Sentinel data for each year has more accuracy; the built-up location fits into their original representation on the HRL imperviousness, and the Corine land cover indicated. However, 2020 shows a bit of mismatch in the area that contains non-irrigated land, pasture, and the construction site. The construction site could easily be mixed up because machinery and other heavy-duty equipment tend to get the land compacted, making it difficult for water to penetrate the soil. The output from the Landsat for all the year still shows a high amount of misclassification; from this, it could be detected 10m resolution gave better classification from the LSMA.

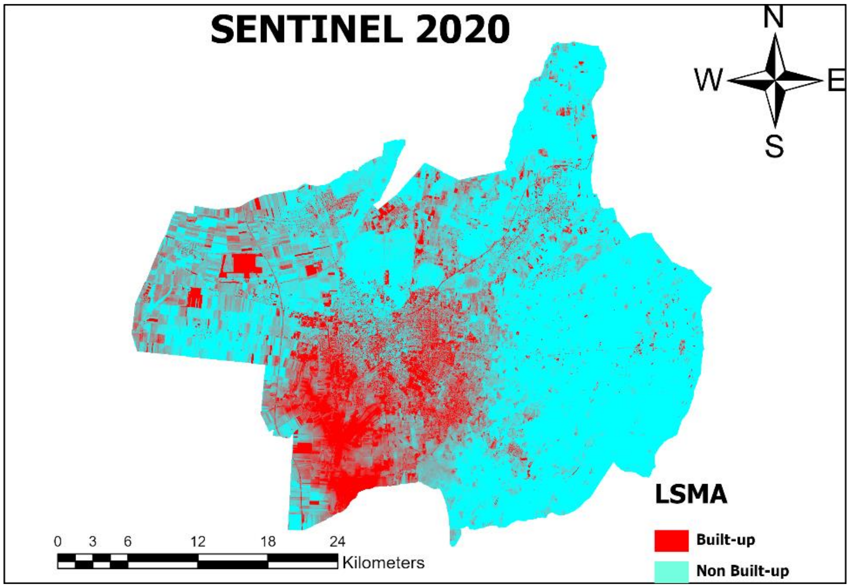

Fig. 12. Non-built up(blue) and Built up(red) extracted from Linear Spectral Mixture analysis for Sentinel 2020.

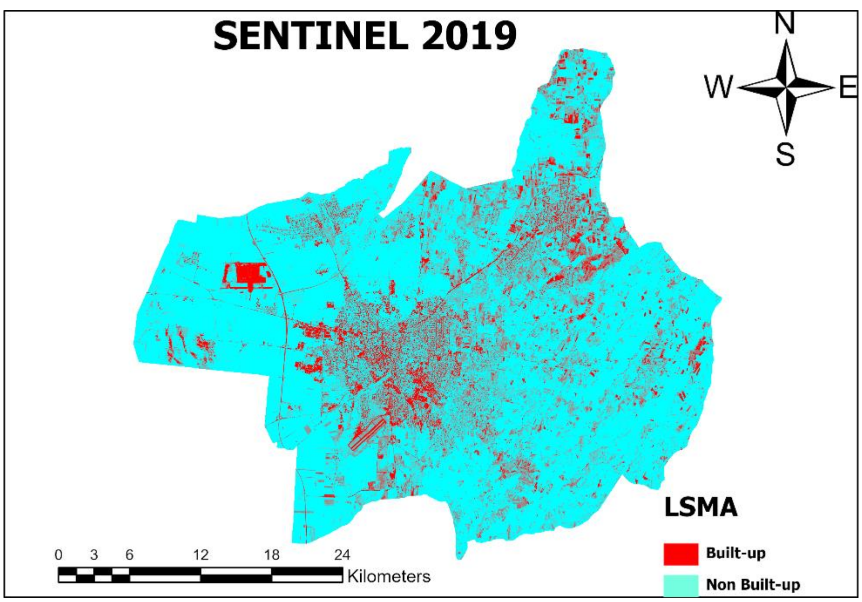

Fig. 13. Non-built up(blue) and Built up(red) extracted from Linear Spectral Mixture analysis for Sentinel 2019.

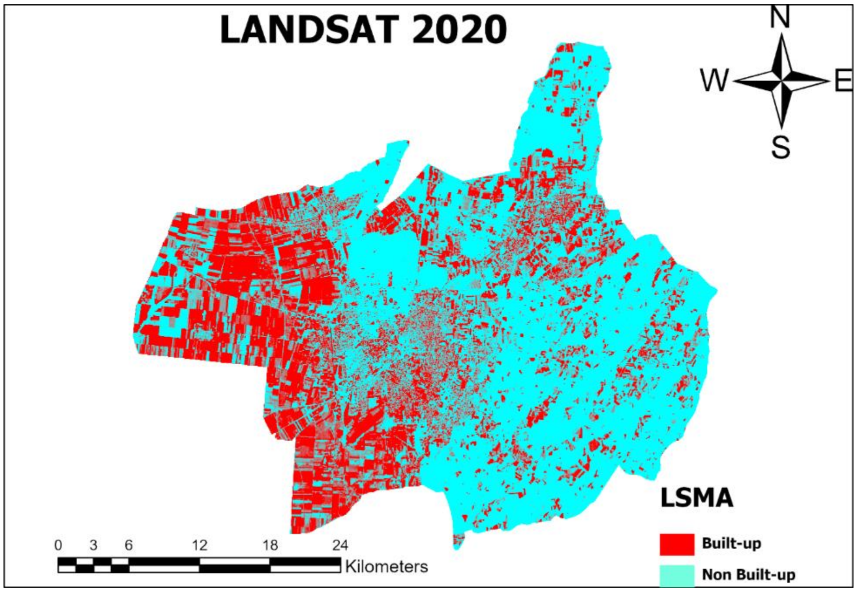

Fig. 14. Non-built up(blue) and Built up(red) extracted from Linear Spectral Mixture analysis for Landsat 2020.

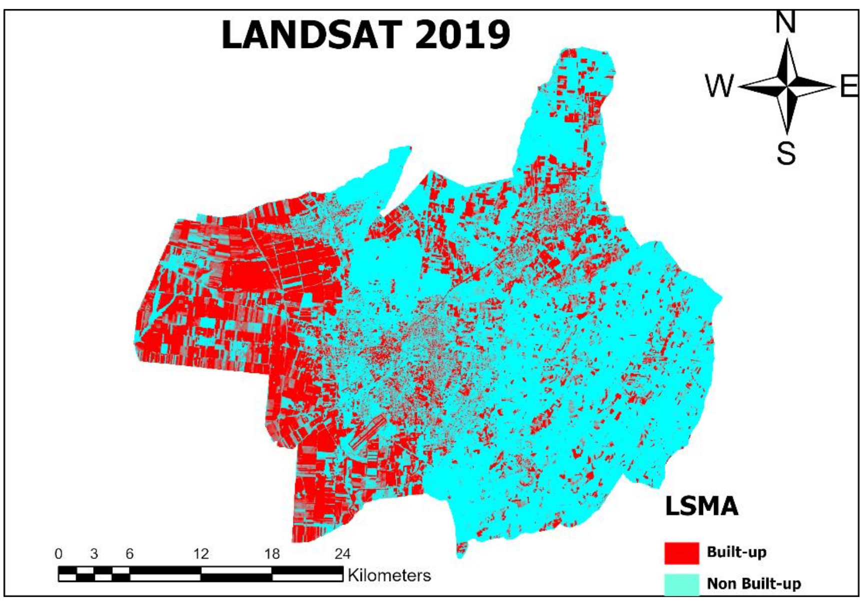

Fig. 15. Non-built up(blue) and Built up(red) extracted from Linear Spectral Mixture analysis for Landsat 2019.

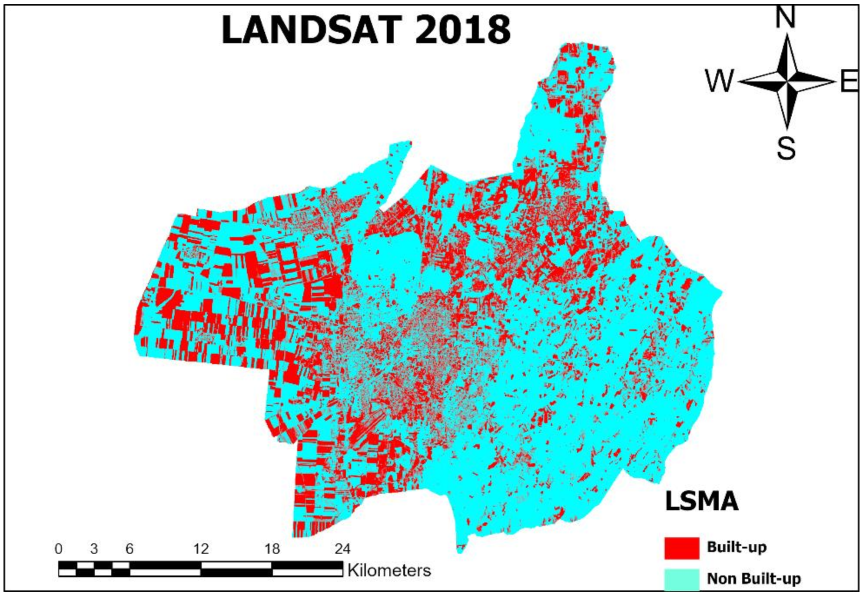

Fig. 16. Non-built up(blue) and Built up(red) extracted from Linear Spectral Mixture analysis for Landsat 2018.

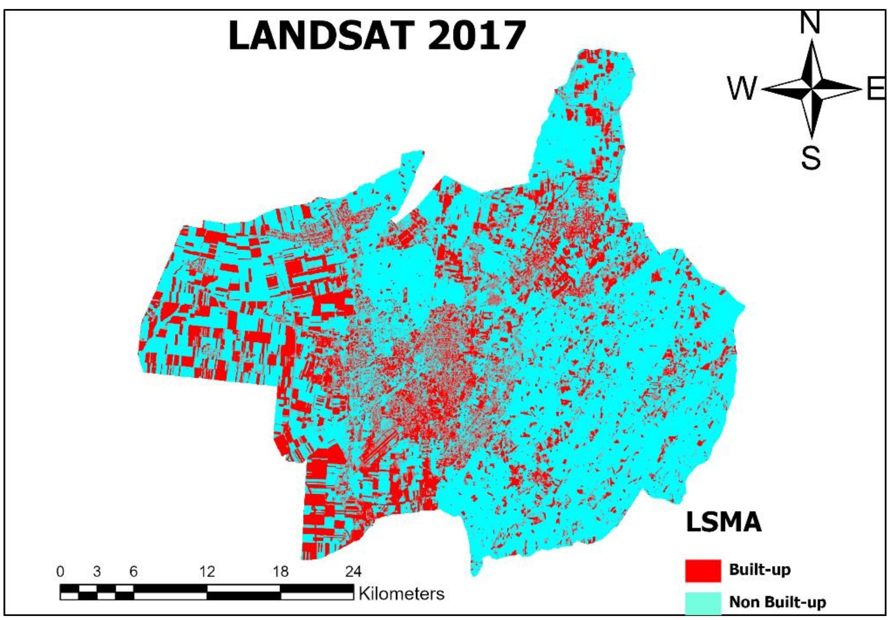

Fig. 17. Non-built up(blue) and Built up(red) extracted from Linear Spectral Mixture analysis for Landsat 2017.

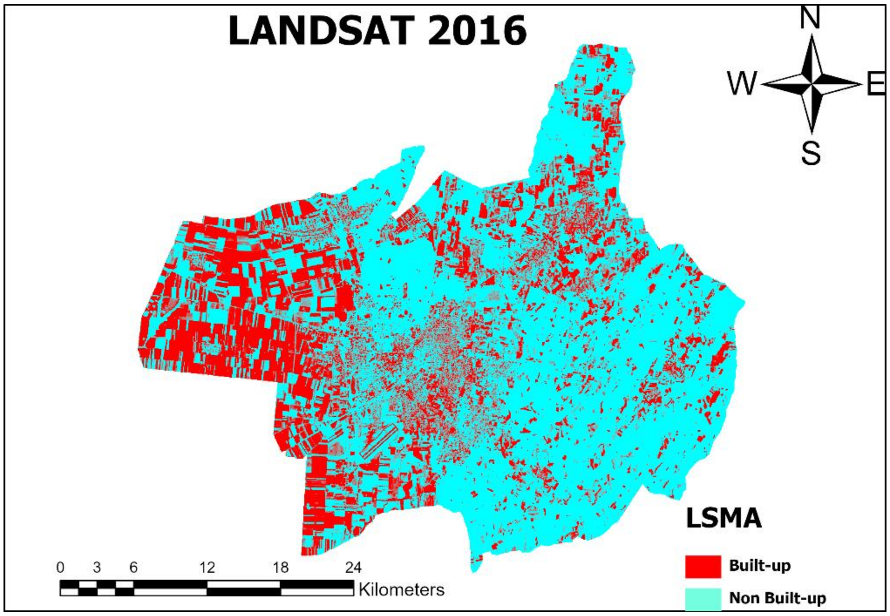

Fig. 18. Non-built up(blue) and Built up(red) extracted from Linear Spectral Mixture analysis for Landsat 2016.

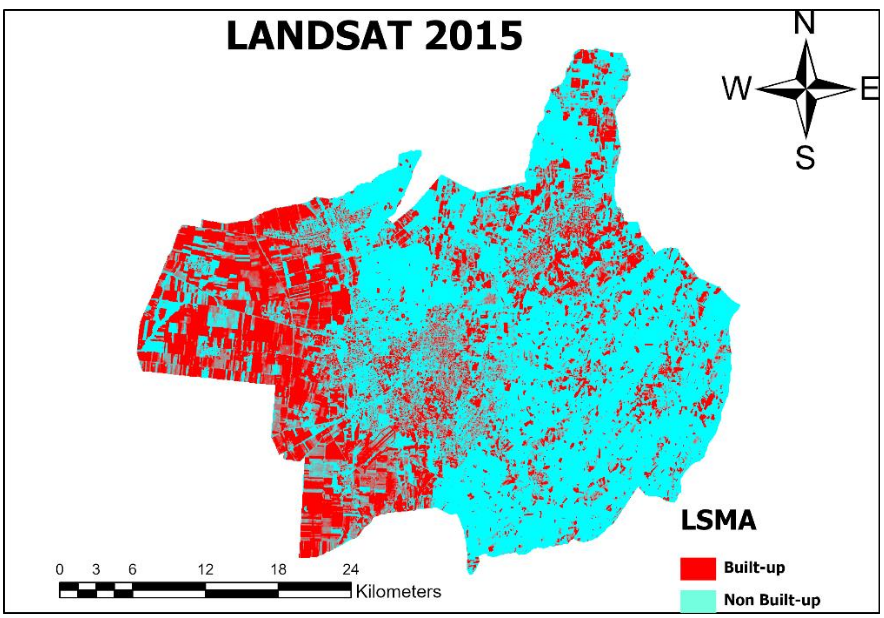

Fig. 19. Non-built up(blue) and Built up(red) extracted from Linear Spectral Mixture analysis for Landsat 2015.

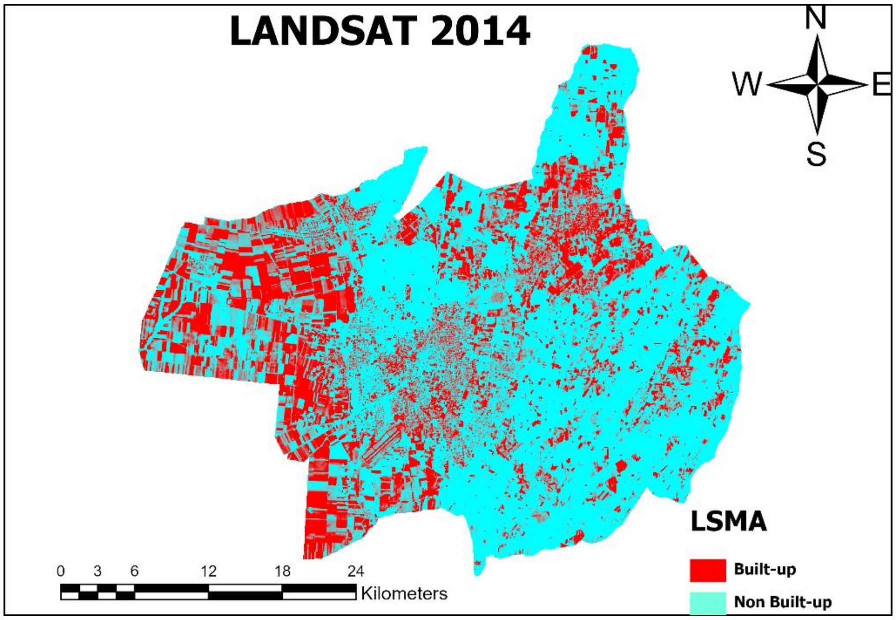

Fig. 20. Non-built up(blue) and Built up(red) extracted from Linear Spectral Mixture analysis for Landsat 2014.

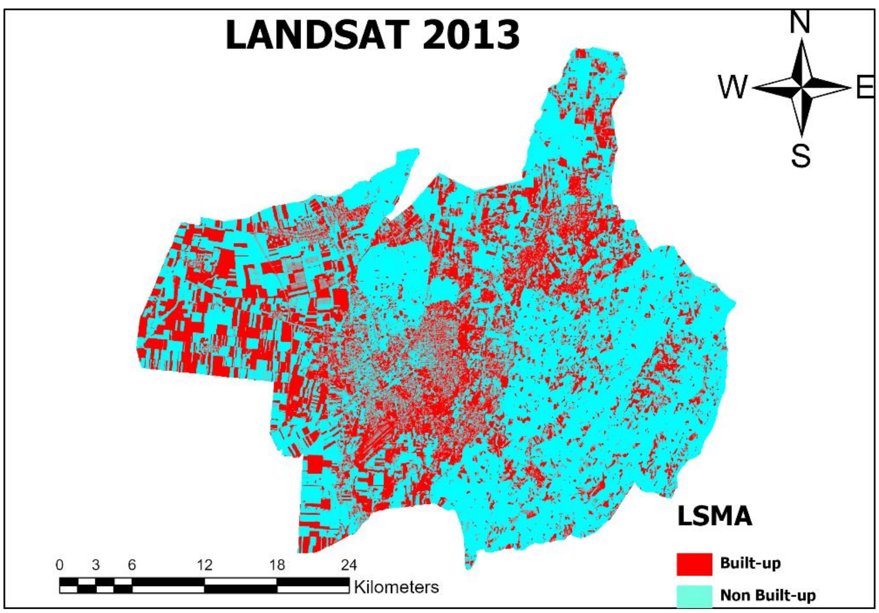

Fig. 21. Non-built up(blue) and Built up(red) extracted from Linear Spectral Mixture analysis for Landsat 2013.

The rate of imperviousness through the linear spectral analysis carried out; the values were further extracted from each pixel using random sampling techniques. From observation and estimation, the data gotten from google earth and that HRL showed a level of similarity. Furthermore, the linear regression was used between each of these carried out against the data from Copernicus HRL imperviousness for validation as indicated in Fig. 22 and 23. The result shows a relatively high correlation of 0.7, and the coefficient of determination is 0.6 for the 2020 sentinel, while the sentinel data for the year 2019 correlates with 0.6, and the coefficient of determination is 0.5. The correlation and coefficient of determination for the Landsat were relatively low. The multiple linear regression carried out on the 10 different datasets showed some levels of similarities between both data of Sentinel and Landsat. It shows a correlation of 0.8, and the coefficient of determination is 0.7.

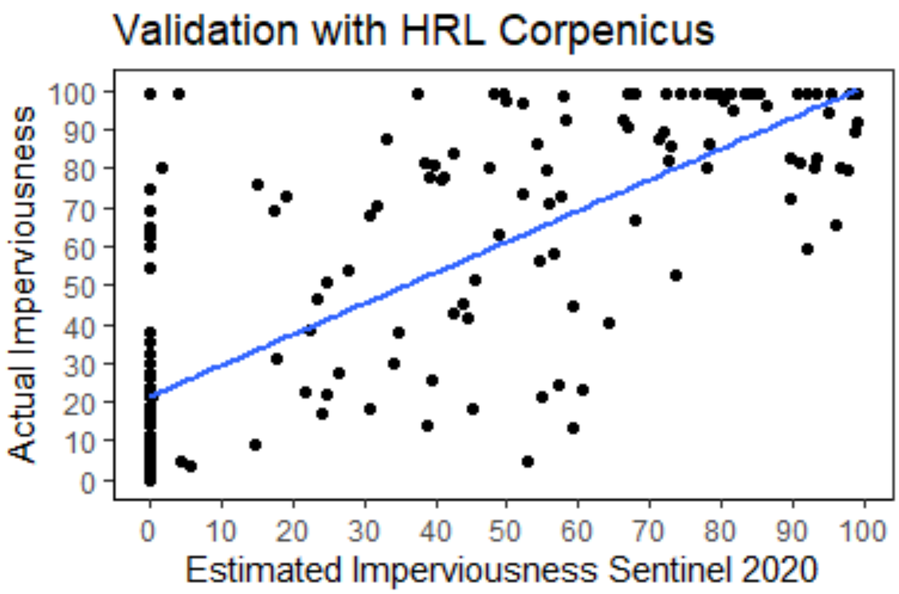

Fig. 22. Regression analysis of Actual imperviousness of HRL Copernicus and Estimated imperviousness for Sentinel 2020.

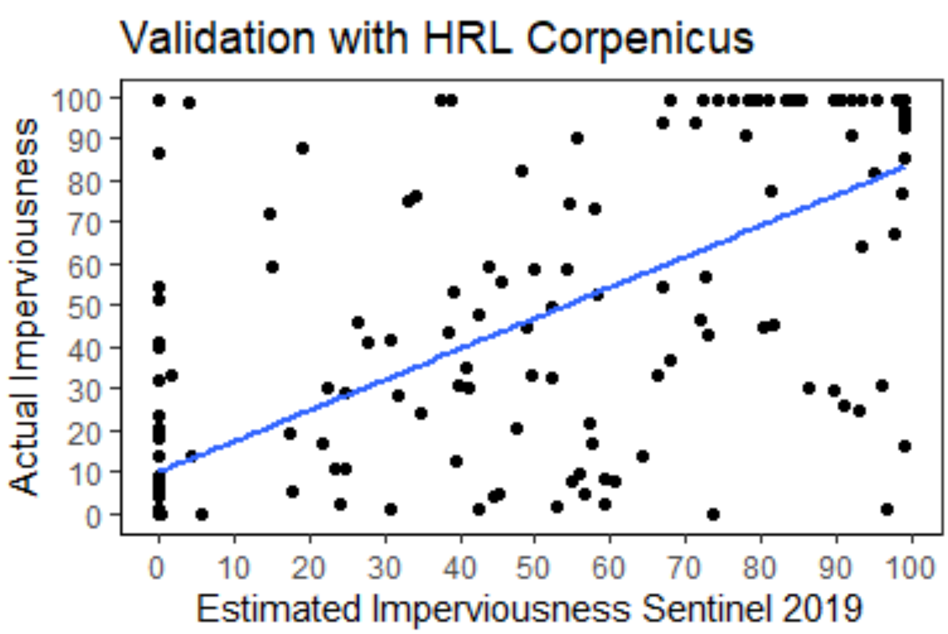

Fig. 23. Regression analysis of Actual imperviousness of HRL Copernicus and Estimated imperviousness for Sentinel 2019.

3.3 Imperviousness rate and the projected stormwater flow.

Based on the result from the regression model, the rate of imperviousness predicted has higher accuracy with the sentinel multispectral imagery data of the year 2020. The model accuracy test is shown in table 3. The Mean Absolute Error (MAE), Mean Square Error (MSE), Root Mean Square Error (RMSE) are the least while the R^2 is the highest for this year. Of the Landsat data, only the 2017 data has a relatively good accuracy compared to the observed data of Copernicus High-Resolution Imperviousness level. The findings by Zhang et al. (2015) showed lower accuracy for LSMA to assess the rate of imperviousness using Landsat ETM+ for a four seasonal period in Cape Town, South Africa, and the accuracy was 55.97%, on the contrary, he used Artificial Neural Network and got an accuracy higher than 80%.

Table 3: The Level of Impervious accuracy check for each of the year

Imperviousness model test	MAE	MSE	RMSE	R^2
Sentinel 2020	0.175	0.059	0.243	0.601
Sentinel 2019	0.204	0.071	0.266	0.521
Landsat 2020	0.291	0.119	0.345	0.196
Landsat 2019	0.273	0.109	0.331	0.26
Landsat 2018	0.275	0.112	0.334	0.243
Landsat 2017	0.221	0.087	0.294	0.414
Landsat 2016	0.259	0.104	0.322	0.296
Landsat 2015	0..274	0.112	0.335	0.242
Landsat 2014	0.269	0.107	0.328	0.273
Landsat 2013	0.258	0.104	0.322	0.299

Xu et al. (2018) findings at the urban area of Guangzhou, China, showed the modified Linear spectral mixture analysis using Sentinel 2A level 1c which was converted to level 2A predicted better. The research was done using the Normalized Difference Vegetation Index and the LSMA, after extracting each of the values, those NDVI lesser than

0.2 were reclassified as an impervious layer. The overall accuracy was found to be 85.7%. In contrast, my research used Copernicus imperviousness data as ground truth for validation, while Xu et al., 2018 exclusively used Google earth.

The level of imperviousness, as shown in Fig. 24, shows the dataset of Sentinel 2020 with the highest accuracy. This shows that the city of Debrecen has a relatively high level of percentage imperviousness most especially in the center of the city. And some of the misclassifications were with locations where tall trees shading an impervious surface, assumption is made based on the proportion, which makes the result show a lower level of imperviousness. In the city, the vegetation growth is good enough as they are well-spaced and situated in strategic places where they cushion the effect of the increasing urbanization. Most of the imperviousness levels between 0-20% are mainly in the outskirt of the city, where there are farms, arable lands, vegetations, and forests.

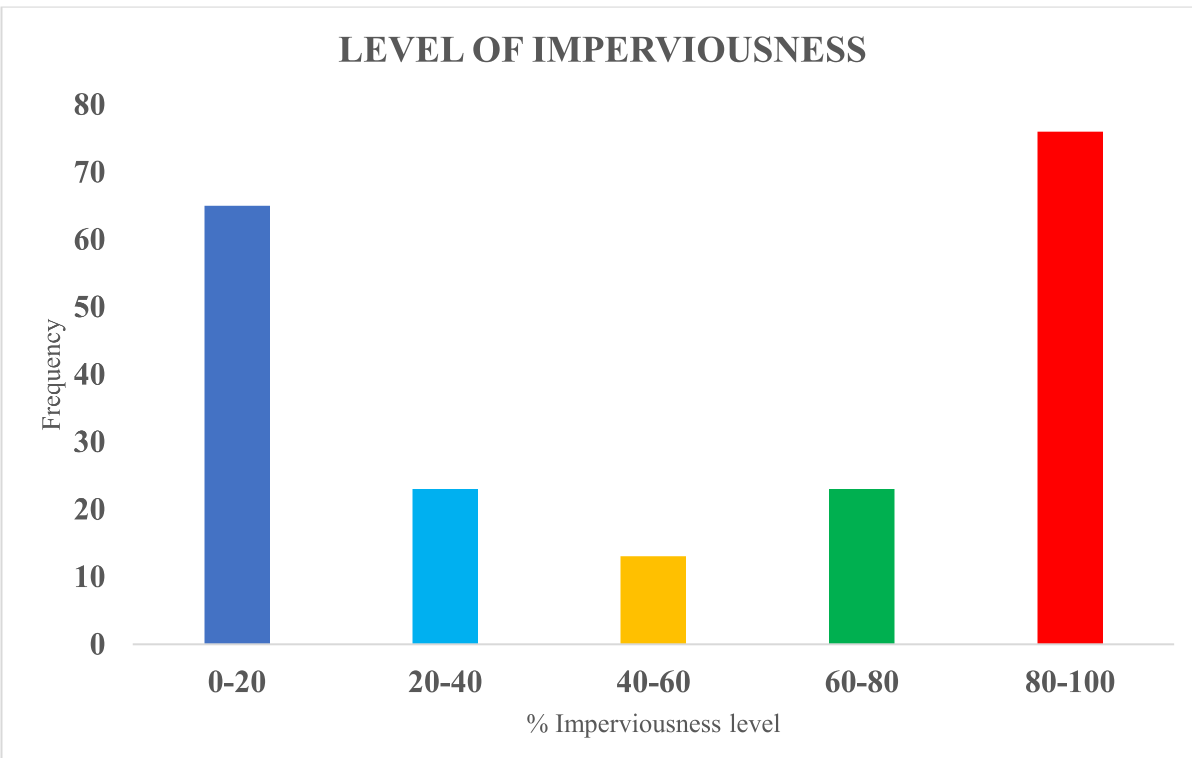

Fig. 24. The estimated percentage level of imperviousness in the city of Debrecen.

In a study conducted by Yang et al. (2010), it was suggested that 35% is the statistical threshold for impervious surface areas that would significantly influence the watershed. Research by Paul and Meyer (2008), Arnold and Gibbons (1996), and the Environmental Protection Agency 1993a indicated that imperviousness level between 10 – 20% would result in reduced infiltration with 20% runoff, 35-50% imperviousness would yield 30% runoff, and 75-100% imperviousness could generate as high as 55% runoff after rainfall. From the result of this research, there is a tendency of 55% runoff in 76 locations of the sampled region, mainly in the center of the city.

CONCLUSIONS

Recent advances in multispectral imaging technology have allowed the release of new imaging devices with improved capabilities. These new gadgets outperform earlier technologies regarding spatial precision, spectral range, and breadth. We can discover new possibilities for geographic analysis in urban development management, water management, and farmland by investigating the possible uses of these new imaging devices.

For this research, one of these cutting-edge imaging devices, the Copernicus Sentinel 2A level 2A, was evaluated for its ability to derive the imperviousness level in the city of Debrecen. Because impervious surfaces restrict water penetration and can cause flooding and other environmental problems, they play an important role in municipal growth management, water management, and environmental protection.

The study found that Sentinel 2A level 2A imagery gave a more precise assessment of imperviousness in Debrecen than the Landsat 8 OLI dataset, the most recent imaging technology available during research. This discovery indicates that Sentinel 2A level 2A imaging technology could benefit environmental surveillance and control, especially in metropolitan regions with impervious surfaces. Overall, this research emphasizes the possible advantages of using new multispectral imaging tools to improve our knowledge and control of the environment.

The study's results are similar to those of He et al., who found limitations with the Normalized Built-Up Index in 2003. (NDBI). The inaccuracies of the NDBI method may be attributed to their higher reflectance levels in the Shortwave Infrared (SWIR) region compared to the Near-Infrared region, which further strengthened the study findings on the NDBI method, resulting in the misclassification of areas with bare land and vegetation, as these areas also had high reflectance levels in the SWIR region. The study also employed a Linear Spectral Mixture Analysis (LSMA) method, which showed promising results in accurately identifying impervious surfaces. However, the LSMA method is still subject to further refinement and improvement to ensure its accuracy and reliability.

The findings showed the limitations of using methods such as the NDBI and the potential of alternative methods, such as LSMA, to determine impervious surfaces correctly. More study is required to enhance and improve these techniques to guarantee their accuracy in finding impervious surfaces and enhancing urban development, water, and farm practices. The LSMA used in the analysis distinguished between built-up and non-built-up areas and was compared to Copernicus' HRL imperviousness; the regression model revealed that Sentinel imagery for 2020 had the highest level of accuracy, with a p-value less than 0.05, R^2 and RMSE of 0.6 and 0.243, respectively.

This study employed a regression model to predict the stormwater flow levels resulting from imperviousness. Impervious surfaces, such as pavement and roofs, prevent water from percolating into the earth, resulting in more significant runoff and stormwater movement. The regression model used in the study established the connection between different imperviousness generated by remote sensing imageries with those also compared to the stormwater discharge volumes.

The study results showed that 38% of the sampled locations in the study area exhibited the highest possible level of imperviousness, which can result in increased stormwater flow levels. On the other hand, 32.5% of the region consisted entirely of pervious surfaces that allow for natural infiltration of water into the ground, leading to decreased stormwater flow levels.

These findings underscore the importance of managing impervious surfaces in Debrecen, Hungary, to minimize the impact of increased stormwater flow levels on the environment and infrastructure. These results can assist urban planners and policymakers in predicting and managing the impact of imperviousness on stormwater flow levels in the area, especially when Debrecen as a city is heavily developing infrastructure.

REFERENCES

1. Akinyemi, F. O., Ikanyeng, M., and Muro, J. (2019). Land cover change effects on land surface temperature trends in an African urbanizing dryland region. City and Environment Interactions, 4, 100029. https://doi.org/10.1016/j.cacint.2020.100029
2. Akter, A., Tanim, A. H., and Islam, M. K. (2020). Possibilities of urban flood reduction through distributed-scale rainwater harvesting. Water Science and Engineering, 13(2), 95–105. https://doi.org/10.1016/j.wse.2020.06.001
3. Anser, M. K., Alharthi, M., Aziz, B., and Wasim, S. (2020). Impact of urbanization, economic growth, and population size on residential carbon emissions in the SAARC countries. Clean Technologies and Environmental Policy, 22(4), 923–936. https://doi.org/10.1007/s10098-020-01833-y
4. Arnold, C. L., and Gibbons, C. J. (1996). Impervious Surface Coverage: The Emergence of a Key Environmental Indicator. Journal of the American Planning Association, 62(2), 243–258. https://doi.org/10.1080/01944369608975688
5. Bates, P. D., and De Roo, A. P. J. (2000). A simple raster-based model for flood inundation simulation. Journal of Hydrology, 236(1–2), 54–77. https://doi.org/10.1016/s0022-1694(00)00278-x
6. Bathurst, J., Birkinshaw, S., Johnson, H., Kenny, A., Napier, A., Raven, S., Robinson J., and Stroud, R. (2018). Runoff, flood peaks and proportional response in a combined nested and paired forest plantation/peat grassland catchment. Journal of Hydrology, 564, 916–927. https://doi.org/10.1016/j.jhydrol.2018.07.039
7. Beyer, H., Merrill, E., Varley, N., and Boyce, M. (2007). Willow on Yellowstone's Northern Range: Evidence for a Trophic Cascade? Ecological Applications, 17(6), 1563-1571. Retrieved December 27, 2020, from http://www.jstor.org/stable/40062057
8. Bradshaw, C. J. A., Sodhi, N. S., Peh, K. S. H., and Brook, B. W. (2007). Global evidence that deforestation amplifies flood risk and severity in the developing world. Global Change Biology, 13(11), 2379–2395. https://doi.org/10.1111/j.1365-2486.2007.01446.x
9. Braud, I., Breil, P., Thollet, F., Lagouy, M., Branger, F., Jacqueminet, C. and Michel, K. (2013). Evidence of the impact of urbanization on the hydrological regime of a medium-sized periurban catchment in France. Journal of Hydrology, 485, 5–23. https://doi.org/10.1016/j.jhydrol.2012.04.049

10. Browne, S., Lintern, A., Jamali, B., Leitão, J. P., and Bach, P. M. (2021). Stormwater management impacts of small urbanising towns: The necessity of investigating the 'devil in the detail.' Science of The Total Environment, 757, 143835. https://doi.org/10.1016/j.scitotenv.2020.143835
11. Carvalho, L., Mackay, E. B., Cardoso, A. C., Baattrup-Pedersen, A., Birk, S., Blackstock, K. L., Borics G, Borja A., Feld C., Ferreira M., Globevnik L., Grizzetti B., Hendry S., Hering D., Kelly M., Langaas S., Meissner K, Pannagopoulos Y., and Solheim, A. L. (2019). Protecting and restoring Europe's waters: An analysis of the future development needs of the Water Framework Directive. Science of The Total Environment, 658, 1228–1238. https://doi.org/10.1016/j.scitotenv.2018.12.255
12. Cerdà, A. (1996). Seasonal variability of infiltration rates under contrasting slope conditions in southeast Spain. Geoderma, 69(3–4), 217–232. https://doi.org/10.1016/0016-7061(95)00062-3
13. Chang, C. I. (2016). Linear Spectral Mixture Analysis. Real-Time Progressive Hyperspectral Image Processing, 37–73. https://doi.org/10.1007/978-1-4419-6187-7_2
14. Chapron, G., Legendre, S., Ferrière, R., Clobert, J., and Haight, R. G. (2003). Conservation and control strategies for the wolf (Canis lupus) in western Europe based on demographic models. Comptes Rendus Biologies, 326(6), 575–587. https://doi.org/10.1016/s1631-0691(03)00148-3
15. Chen, J., Hill, A. A., and Urbano, L. D. (2009). A GIS-based model for urban flood inundation. Journal of Hydrology, 373(1–2), 184–192. https://doi.org/10.1016/j.jhydrol.2009.04.021
16. Cole, B., Smith, G., and Balzter, H. (2018). Acceleration and fragmentation of CORINE land cover changes in the United Kingdom from 2006–2012 detected by Copernicus IMAGE2012 satellite data. International Journal of Applied Earth Observation and Geoinformation, 73, 107–122. https://doi.org/10.1016/j.jag.2018.06.003
17. D'Acci, L. S. (2021). Preferring or Needing Cities? (Evolutionary) psychology, utility and life satisfaction of urban living. City, Culture and Society, 24, 100375. https://doi.org/10.1016/j.ccs.2021.100375
18. Davis, K. (1955). The Origin and Growth of Urbanization in the World. American Journal of Sociology, 60(5), 429-437. Retrieved December 27, 2020, from http://www.jstor.org/stable/2772530
19. Dreelin, E. A., Fowler, L., and Ronald Carroll, C. (2006). A test of porous pavement effectiveness on clay soils during natural storm events. Water Research, 40(4), 799–805. https://doi.org/10.1016/j.watres.2005.12.002

20. Duan, S.-B., Li, Z.-L., Cheng, J., & Leng, P. (2017). Cross-satellite comparison of operational land surface temperature products derived from MODIS and ASTER data over bare soil surfaces. ISPRS Journal of Photogrammetry and Remote Sensing, 126, 1–10. https://doi.org/10.1016/j.isprsjprs.2017.02.003
21. Ekka, S. A., Rujner, H., Leonhardt, G., Blecken, G.-T., Viklander, M., and Hunt, W. F. (2021). Next generation swale design for stormwater runoff treatment: A comprehensive approach. Journal of Environmental Management, 279, 111756. https://doi.org/10.1016/j.jenvman.2020.111756
22. Environmental Protection Agency. (1993a). Guidance Specifying Management Measures for Sources of Nonpoint Source Pollution in Coastal Waters United States Environmental Protection Agency #840-B-92-002. Washington, DC: USEPA Office of Water.
23. Ercolani, G., Chiaradia, E. A., Gandolfi, C., Castelli, F., and Masseroni, D. (2018). Evaluating performances of green roofs for stormwater runoff mitigation in a high flood risk urban catchment. Journal of Hydrology, 566, 830–845. https://doi.org/10.1016/j.jhydrol.2018.09.050
24. Estoque, R. C., and Murayama, Y. (2015). Classification and change detection of built-up lands from Landsat-7 ETM+ and Landsat-8 OLI/TIRS imageries: A comparative assessment of various spectral indices. Ecological Indicators, 56, 205–217. https://doi.org/10.1016/j.ecolind.2015.03.037
25. Gopalakrishnan, R., Seppänen, A., Kukkonen, M., and Packalen, P. (2020). Utility of image point cloud data towards generating enhanced multitemporal multisensor land cover maps. International Journal of Applied Earth Observation and Geoinformation, 86, 102012. https://doi.org/10.1016/j.jag.2019.102012
26. Hawley, R. J., and Bledsoe, B. P. (2011). How do flow peaks and durations change in suburbanizing semi-arid watersheds? A southern California case study. Journal of Hydrology, 405(1–2), 69–82. https://doi.org/10.1016/j.jhydrol.2011.05.011
27. He, C., Shi, P., Xie, D., & Zhao, Y. (2010). Improving the normalized difference built-up index to map urban built-up areas using a semiautomatic segmentation approach. Remote Sensing Letters, 1(4), 213–221. https://doi.org/10.1080/01431161.2010.481681
28. He, C., Shi, P., Xie, D., & Zhao, Y. (2010). Improving the normalized difference built-up index to map urban built-up areas using a semiautomatic segmentation approach. Remote Sensing Letters, 1(4), 213–221. https://doi.org/10.1080/01431161.2010.481681

29. Hoang, N. D. (2021). Automatic Impervious Surface Area Detection Using Image Texture Analysis and Neural Computing Models with Advanced Optimizers. *Computational Intelligence and Neuroscience*, *2021*, 1–17. https://doi.org/10.1155/2021/8820116

30. Horváth, Á., Ács, F., and Breuer, H. (2009). On the relationship between soil, vegetation and severe convective storms: Hungarian case studies. Atmospheric Research, 93(1–3), 66–81. https://doi.org/10.1016/j.atmosres.2008.10.007

31. Horváth, Á., Geresdi, I., Németh, P., Csirmaz, K., and Dombai, F. (2009). Numerical modeling of severe convective storms occurring in the Carpathian Basin. Atmospheric Research, 93(1–3), 221–237. https://doi.org/10.1016/j.atmosres.2008.10.019

32. Hyndman, R., Koehler, A., Ord, K., and Snyder, R. (2008). Forecasting with Exponential Smoothing. Springer Series in Statistics, 1–362. https://doi.org/10.1007/978-3-540-71918-2

33. Janus, J. ł., Bożek, P., Mitka, B., Taszakowski, J. ł., and Doroż, A. (2021). Long-term forest cover and height changes on abandoned agricultural land: An assessment based on historical stereometric images and airborne laser scanning data. Ecological Indicators, 120, 106904. https://doi.org/10.1016/j.ecolind.2020.106904

34. Jyoti P. Vibhooti S. (1995) Urbanization, energy use and greenhouse effects in economic development: Results from a cross-national study of developing countries, 5(2), 87-103 https://doi.org/10.1016/0959-3780(95)00015-G

35. Kebede, Y. S., Endalamaw, N. T., Sinshaw, B. G., & Atinkut, H. B. (2021). Modeling soil erosion using RUSLE and GIS at watershed level in the upper beles, Ethiopia. Environmental Challenges, 2, 100009. https://doi.org/10.1016/j.envc.2020.100009

36. Kookana, R. S., Drechsel, P., Jamwal, P., and Vanderzalm, J. (2020). Urbanisation and emerging economies: Issues and potential solutions for water and food security. Science of The Total Environment, 732, 139057. https://doi.org/10.1016/j.scitotenv.2020.139057

37. Kuc, G., & Chormański, J. (2019). Sentinel-2 Imagery for Mapping and Monitoring Imperviousness in Urban Areas. The International Archives of the Photogrammetry, Remote Sensing and Spatial Information Sciences, XLII-1/W2, 43–47. https://doi.org/10.5194/isprs-archives-xlii-1-w2-43-2019

38. Kumar, S., Shwetank, and Jain, K. (2020). A Multi-Temporal Landsat Data Analysis for Land-use/Land-cover Change in Haridwar Region using Remote Sensing Techniques. Procedia Computer Science, 171, 1184–1193. https://doi.org/10.1016/j.procs.2020.04.127
39. Lakshmi, S. V., James, J., Soundariya, S., Vishalini, T., and Pandian, P. K. (2015). A Comparison of Soil Texture Distribution and Soil Moisture Mapping of Chennai Coast using Landsat ETM+ and IKONOS Data. Aquatic Procedia, 4, 1452–1460. https://doi.org/10.1016/j.aqpro.2015.02.188
40. Leridon, H. (2008). Human populations and climate: Lessons from the past and future scenarios. Comptes Rendus Geoscience, 340(9–10), 663–669. https://doi.org/10.1016/j.crte.2008.06.005
41. Li, W., Niu, Z., Shang, R., Qin, Y., Wang, L., and Chen, H. (2020). High-resolution mapping of forest canopy height using machine learning by coupling ICESat-2 LiDAR with Sentinel-1, Sentinel-2 and Landsat-8 data. International Journal of Applied Earth Observation and Geoinformation, 92, 102163. https://doi.org/10.1016/j.jag.2020.102163
42. Ma, Y., Zhang, S., Yang, K., and Li, M. (2021). Influence of spatiotemporal pattern changes of impervious surface of urban megaregion on thermal environment: A case study of the Guangdong – Hong Kong – Macao Greater Bay Area of China. Ecological Indicators, 121, 107106. https://doi.org/10.1016/j.ecolind.2020.107106
43. McGrane, S. J. (2016). Impacts of urbanisation on hydrological and water quality dynamics, and urban water management: a review. Hydrological Sciences Journal, 61(13), 2295–2311. https://doi.org/10.1080/02626667.2015.1128084
44. Nowak, D. J., and Greenfield, E. J. (2020). The increase of impervious cover and decrease of tree cover within urban areas globally (2012–2017). Urban Forestry & Urban Greening, 49, 126638. https://doi.org/10.1016/j.ufug.2020.126638
45. Obiahu, O. H., and Elias, E. (2020). Effect of land use land cover changes on the rate of soil erosion in the Upper Eyiohia river catchment of Afikpo North Area, Nigeria. Environmental Challenges, 1, 100002. https://doi.org/10.1016/j.envc.2020.100002
46. OECD (2018). Regions and Cities at a glance 2018 – Hungary Retrieved December 27, 2020, from https://www.oecd.org/regional/HUNGARY-Regions-and-Cities-2018.pdf
47. Otsu, N. (1979). A Threshold Selection Method from Gray-Level Histograms. IEEE Transactions on Systems, Man, and Cybernetics, 9(1), 62–66. https://doi.org/10.1109/tsmc.1979.4310076

48. Paul, M. J., and Meyer, J. L. (2008). Streams in the Urban Landscape. Urban Ecology, 207–231. https://doi.org/10.1007/978-0-387-73412-5_12

49. Prasada Mohapatra, R., & Wu, C. (2007). Subpixel Imperviousness Estimation with IKONOS Imagery. Remote Sensing Applications Series. Published. https://doi.org/10.1201/9781420043754.ch2

50. Saniewska, D., Bełdowska, M., Bełdowski, J., Saniewski, M. ł., Szubska, M., Romanowski, A., and Falkowska, L. (2014). The impact of land use and season on the riverine transport of mercury into the marine coastal zone. Environmental Monitoring and Assessment, 186(11), 7593–7604. https://doi.org/10.1007/s10661-014-3950-z

51. Sekertekin, A., & Zadbagher, E. (2021). Simulation of future land surface temperature distribution and evaluating surface urban heat island based on impervious surface area. Ecological Indicators, 122, 107230. https://doi.org/10.1016/j.ecolind.2020.107230

52. Seto, K. C., Guneralp, B., and Hutyra, L. R. (2012). Global forecasts of urban expansion to 2030 and direct impacts on biodiversity and carbon pools. Proceedings of the National Academy of Sciences, 109(40), 16083–16088. https://doi.org/10.1073/pnas.1211658109

53. Steffy, L. Y., and Kilham, S. S. (2006). Effects of urbanization and land use on fish communities in Valley Creek watershed, Chester County, Pennsylvania. Urban Ecosystems, 9(2), 119–133. https://doi.org/10.1007/s11252-006-7901-5

54. Wang, Z., Zhang, S., Peng, Y., Wu, C., Lv, Y., Xiao, K., Zhao J., Qian, G. (2020). Impact of rapid urbanization on the threshold effect in the relationship between impervious surfaces and water quality in shanghai, China. Environmental Pollution, 267, 115569. https://doi.org/10.1016/j.envpol.2020.115569

55. Wauters, R. (2017). Migrants in the midst of city life: spatial patterns and arrival logics of foreign newcomers to Brussels in 1880. Journal of Historical Geography, 58, 39–52. https://doi.org/10.1016/j.jhg.2017.09.004

56. Wei, C., & Blaschke, T. (2018). Pixel-Wise vs. Object-Based Impervious Surface Analysis from Remote Sensing: Correlations with Land Surface Temperature and Population Density. Urban Science, 2(1), 2. https://doi.org/10.3390/urbansci2010002

57. Weigand, M., Staab, J., Wurm, M., and Taubenböck, H. (2020). Spatial and semantic effects of LUCAS samples on fully automated land use/land cover classification in high-resolution Sentinel-2 data. International Journal of Applied Earth Observation and Geoinformation, 88, 102065. https://doi.org/10.1016/j.jag.2020.102065

58. Wenger, S. J., Roy, A. H., Jackson, C. R., Bernhardt, E. S., Carter, T. L., Filoso, S., Gibson A, Hession C, Kaushal S., Martí E., Meyer J., Palmer M., Paul M., Purcell A., Ramírez A., Rosemond A., Schofield K., Sudduth E., Walsh, C. J. (2009). Twenty-six key research questions in urban stream ecology: an assessment of the state of the science. Journal of the North American Benthological Society, 28(4), 1080–1098. https://doi.org/10.1899/08-186.1

59. Xu, J., Zhao, Y., Zhong, K., Ruan, H., and Liu, X. (2016). Coupling Modified Linear Spectral Mixture Analysis and Soil Conservation Service Curve Number (SCS-CN) Models to Simulate Surface Runoff: Application to the Main Urban Area of Guangzhou, China. Water, 8(12), 550. https://doi.org/10.3390/w8120550

60. Xu, R., Liu, J., and Xu, J. (2018). Extraction of High-Precision Urban Impervious Surfaces from Sentinel-2 Multispectral Imagery via Modified Linear Spectral Mixture Analysis. Sensors, 18(9), 2873. https://doi.org/10.3390/s18092873

61. Yang, X. G., W. Y. Fan, and Y. Yu. 2010. Estimation of forest canopy chlorophyll content based on PROSPECT and SAIL models. Spectroscopy and Spectral Analysis. https://doi.org/10.3964/j.issn.1000-0593(2010)11-3022-05.

62. Zhang, Y., Lin, H., Zhang, Y., & Weng, Q. (2015). Remote Sensing of Impervious Surfaces in Tropical and Subtropical Areas. Amsterdam, Netherlands: Amsterdam University Press